Pulsar Based Timing for Grid Synchronization

Wei Qiu, *Student Member, IEEE*, He Yin, *Member, IEEE*, Liang Zhang, Xiqian Luo, Weikang Wang, Yilu Liu, *Fellow, IEEE*, Wenxuan Yao, *Senior Member, IEEE*, Lingwei Zhan, Peter L. Fuhr, *Senior Member, IEEE*, and Thomas J King Jr

***Abstract*—Existing synchronization systems in the power grid, such as the global positioning system, are susceptible to temporary or permanent failures due to various unpredictable and uncontrollable factors such as cyber-attack and electromagnetic interferences, thus affecting the accuracy and reliability of generated timing signal. In this article, a pulsar astronomy-based timing system is proposed to provide an alternative synchronization signal. This clock will offer significant security improvements to power grid applications, such as a wide-area monitoring system, which depends on a precise timing signal. The hardware and software frameworks are described in detail. First, a high-speed sampling hardware platform is designed to collect signals from radio telescopes. Then a periodic pulse extraction method with three steps is proposed to process the pulsar signal, including polyphase filterbanks, incoherent de-dispersion, and sliding window folding. Lastly, three experiments are conducted to verify the effectiveness of the frameworks. The generated pulsar timing pulse is presented, and the factors affecting its accuracy are also discussed. The analysis results demonstrate that the pulsar signals can provide high-accurate timing pulses for grid synchronization.**

***Index Terms*—High-speed sampling hardware, periodic pulse extraction method (PPEM), pulsar astronomy, timing system.**

Manuscript received July 23, 2020; revised October 27, 2020 and December 26, 2020; accepted January 2, 2021. Date of publication February 4, 2021; date of current version May 19, 2021. Paper 2020-PSEC-0956.R2, presented at the 2020 IAS Annual Meeting, Detroit, MI, USA, Oct. 10–16, and approved for publication in the IEEE TRANSACTIONS ON INDUSTRY APPLICATIONS by the Power Systems Engineering Committee of the IEEE Industry Applications Society. This work was supported in part by the Major Research Instrumentation Program of the National Science Foundation under the Award 1920025, in part by the Engineering Research Center program of the National Science Foundation under NSF Award EEC-1920025, and in part by the Department of Energy and the CURENT Industry Partnership Program. *(Corresponding author: Wenxuan Yao.)*

Wei Qiu is with the Department of Electrical Engineering, and Computer Science, University of Tennessee, Knoxville, TN 37996, USA, and also with the College of Electrical and Information Engineering, Hunan University, Changsha 410082, China (e-mail: qwei4@utk.edu).

He Yin, Liang Zhang, Xiqian Luo, and Weikang Wang are with the Department of Electrical Engineering and Computer Science, University of Tennessee, Knoxville, TN 37996 USA (e-mail: hyin8@utk.edu; lzhan104@utk.edu; xluo18@utk.edu; wwang72@vols.utk.edu).

Yilu Liu is with the Department of Electrical Engineering and Computer Science, University of Tennessee, Knoxville, TN 37996, USA, and also with Oak Ridge National Laboratory, Oak Ridge, TN 37830 USA (e-mail: liu@utk.edu).

Wenxuan Yao is with the College of Electrical and Information Engineering, Hunan University, Changsha 410082, China (e-mail: ywxhnu@gmail.com).

Lingwei Zhan, Peter L. Fuhr, and Thomas J King Jr are with the Oak Ridge National Laboratory, Oak Ridg, TN, 37830 USA (e-mail: zhanl@ornl.gov; fuhrpl@ornl.gov; kingtjjr@ornl.gov).

Color versions of one or more figures in this article are available at https://doi.org/10.1109/TIA.2021.3057352.

Digital Object Identifier 10.1109/TIA.2021.3057352

I. Introduction

ACCURATE timing is a prerequisite for the power grid's monitoring and control. For example, the phasor measurement units (PMUs) leverage high precision pulse per second (PPS) with nanosecond level from global positioning system (GPS) satellite for time synchronization and provides current and voltage phasor measurements to monitor the status of the power grid [1], [2]. However, the timing security, and reliability provided by GPS receivers are threatened by various factors including system failures, space weather, jamming, and cyber-attacks such as GPS spoofing [3]. For example, in 2013, an $ 80 million yacht was hijacked and controlled by making the spoofing GPS signals [4]. Additionally, a GPS loss study on commercial PMUs has concluded that more than 50% of the PMUs have experienced frequent GPS signal loss issues [5]. As a result, the GPS dependent timing system is susceptible to external interference, which can cause tremendous measurement errors as timing directly determines the measurement reliability and accuracies [6], [7]. For instance, the GPSs timing signal provided to power measurement systems can reach 100 ns in theory via PPS signals [8]. The satellite receivers cannot lock to time signals, causing larger synchronous measurement errors [9]. According to IEEE Standard C37.118.1-2011 [10], a timing error of 26 μs in a 60 Hz power system can cause 1% total vector error, which reaches the limits of its accuracy requirement [11].

To address this problem, some calibration methods are used to reduce clock errors. For example, the absolute calibration method is performed using the GPS HW simulator [12]. This absolute calibration is not practical since it is time-consuming. Meanwhile, an absolute calibration method for two signal bands in Galileo timing receivers is developed based on a hardware simulator [13]. The absolute calibration requires a very accurate delay between the radio frequency signal from global navigation satellite systems (GNSS) and the 1 PPS timing signal. This means that additional cables and adaptors are necessary. It is claimed that about 0.4 ns accuracy can be achieved for the receiver of GPS [14]. However, it is not allowed for the absolute calibration method that the hardware delays of the already operational receivers which may not be interrupted.

Therefore, the relative calibration is further proposed to calibrate the Galileo receiver [15]. The relative calibration approach is based on the comparison between the measurements from the local receiver and the reference receiver that is already calibrated. In this case, the hardware delays are determined by the difference between the GNSS time and the independent

calibrated time transfer [16]. Based on this consideration, an accurate two-way satellite time and frequency transfer technique can be used for coordinated universal time (UTC) time transfer [17]. Additionally, a constrained least square analysis is performed for calibration using the data from GPS and GLObal NAvigation Satellite System (GLONASS). Nevertheless, it is necessary to know the prior information of station hardware delays so that the calibration can be developed for the receiving station.

Besides the calibration methods, several methods based on alternative timing sources are proposed so as to reduce the impact of synchronization errors. For example, a compensation method is proposed to correct angle drift when the GPS signal is lost using the local crystal oscillator [11]. However, the crystals oscillator is prone to have large offsets without calibration. Moreover, a chip-scale atomic clock is utilized as a backup clock of the GPS timing signal [18]. Nevertheless, the chip scale atomic clock needs to be disciplined using the GPS signal and has 1 μs timing error in 24 hours. Next, the distributed multi-receiver GPS spoofing detection countermeasure is proposed to eliminate the effects of spoofing [19], [20]. This method is not universally applicable because it requires multiple receivers to coordinate.

Alternatively, it has been found that accurate periodic signals can be emitted by the neutron star (pulsar) rotating at high speed, which is essentially a radio wave beam. The typical deviation of rotation periods is extremely small, which can reach 10^{-18} second per second for young pulsars [21]. For instance, the millisecond pulsar pulsating source of radio (PSR) B1937+21 has a rotation period of 1.557 ms within an error of $10^{-17}s$ [22], where B denotes the pulsar has a binary companion. To observe pulsar signals, many different sizes of radio telescopes have been made. For example, the world's largest single-aperture radio telescope FAST was built in 2016 [23], and many new pulsars have been observed. Some other radio telescopes, such as square kilometer array (SKA) [24] and hydrogen epoch of reionization array (HERA) [25], have also been built to discover new stars in the universe [26].

Compared with the GPS timing system, the pulsar-based based timing system can reduce the possibility of system failures, space weather, and cyber attack. The detailed reasons can be summarized as follows. For the GPS-based timing system, 1) first, the receiver is recommended to be placed in an unobstructed place otherwise it will fail to receive the GPS RF signal occasionally. 2) Second, primary space weather impacts the stability of GPS signal including range/positioning errors and loss of signal reception. The GPS signal will be lost due to the decreased number of useable satellites [27]. 3) Third, GPS spoofing usually happens when the adversary uses a radio transmitter to send a counterfeit GPS signal to a receiver antenna to counter a legitimate GPS satellite signal [3]. Most navigation systems will prefer to select the strongest GPS signal. Therefore, the fake GPS signal can override the weaker but legitimate satellite signal. The attacker could transmit no data at all or transmit inaccurate coordinates.

For a pulsar-based timing system, 1) First, the system failures can be effectively avoided because the radio telescope is usually installed in a wide-open place outside. Importantly, there is no need to deploy a radio telescope for each PMU because the accurate timing signal can be transmitted to each PMU through the PTP technology [28]. 2) Second, the receiver of the GPS signal is mainly range 1575 and 1227 MHz [29]. The working frequency of a radio telescope receiver is usually wider for a pulsar signal receiver. For example, the Skynet 20 m can provide observations at 1.3 to 1.8 GHz and 8 to 10 GHz [30]. And the Green Bank Telescope 100 m provides unprecedented sensitivity across the telescope's full 0.1– 116 GHz (3.0 m-2.6 mm) operating range [31]. A wider frequency range can ensure that some signals pass through the atmosphere even under the influence of bad weather. Therefore, it has better adaptability compared to GPS receivers. 3) Meanwhile, the GPS spoofing can be avoided since the radio telescope can search for multiple pulsars and the period of the pulsar can be considered fixed. And the radio telescope is not searching for the strongest signal as its target signal, this is also different from the GPS receiver. Therefore, it is impossible to implement an attack similar to GPS spoofing.

Recently, there have been some applications that use pulsars, such as the pulsar-based positioning system. Combine accurate timing and positioning requirements, the pulsar positioning system is introduced in [32] and [33], the relative position can be estimated in three dimensional space after comparing the pulsar signals from three or more pulsars. However, more than three pulsars are required, and the 1 μs timing error can meet the requirements for a pulsar-based positioning system [33]. This will exceed the demand of the power system because a 100 ns error is recommended according to IEEE Std C37.118 [34]. Therefore, it is a new challenge for using this highly accurate pulse signal in a wide area measurement system.

Since the pulsar has the potential to be an accurate timing source, this article first proposes a pulsar-based timing design, and then investigates the feasibility of leveraging pulsar signal for grid synchronization. This article is an extension of the IAS conference paper in [35]. The contribution of this article can be summarized as follows.

1) To obtain the precise timing signal, a high-speed sampling hardware platform is designed to collect and transmit the radio frequency (RF) signal from radio telescopes. This hardware platform has three high-speed analog-to-digital converters (ADCs) (each has four channels) and two high-speed data transmission interfaces.
2) Using the collected pulse data, a periodic pulse extraction method (PPEM) is proposed to extract the stable periodic pulse signal. In PPEM, the polyphase filterbank is used to decompose the pulse signal into multiple frequency bands. Then the periodic pulse can be calculated through the de-dispersion and folding technologies.
3) To verify the effectiveness of the designed hardware, real-time hardware acquisition experiments are conducted. In addition to testing the hardware platform, the simulation and two actual pulse signal cases are used to verify the PPEM. The experimental results show that the effective and accurate pulse signal can be extracted by using the proposed method.

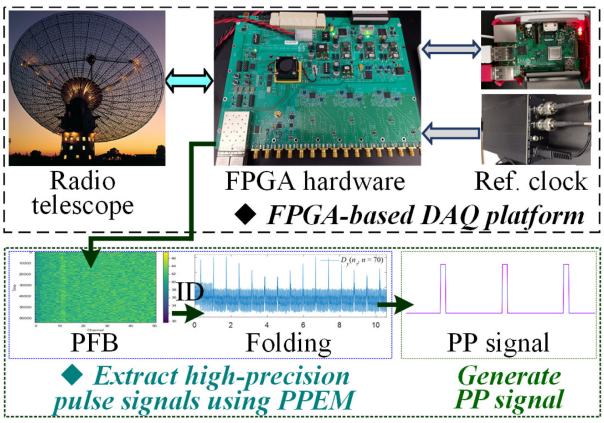

Fig. 1. Pulsar-based timing framework.

4) Compared with the PPS signal from GPS, the timing accuracy of the periodic pulse extracted from the pulsar is relatively higher. Meanwhile, the GPS spoofing, where the counterfeit GPS signal overrides the true satellite signal, can be avoided due to different mechanisms of acquiring signals.

The remainder of this article is organized as follows. Section II introduces the high sample rate data acquisition (DAQ) platform. In Section III, the pulsar signal processing methods are proposed to generate the periodic pulse (PP) signals. Several experiments are then conducted to verify the framework in Section IV. Finally, the experimental results are presented in Section V.

II. Development of Pulsar Signal Acquisition

A. Pulsar Based Timing Framework

Pulsar periods range from the level of microseconds to seconds, thus a high sampling rate DAQ platform is required to detect pulsar signals. The designed pulsar timing system is depicted in Fig. 1. According to the characteristics of different radio telescopes, multichannel ADCs are first used to sample RF signals in the first stage. Then, to process high-speed signals, the field-programmable gate array (FPGA)-based DAQ hardware with hundreds of digital signal processing (DSP) slices are used. In the second stage, the pulse signal can be generated using the proposed PPEM. Referring to this framework, the hardware is designed in detail.

B. Primary Hardware Components

In the field of highly sampled digital signals, some sampling and CPU modules have been designed. The interconnect break-out board (IBOB) and reconfigurable open architecture computing hardware (ROACH) boards are two of the early hardware platforms [36], which have been developed by the collaboration for astronomy signal processing and electronics research (CASPER)[1] group since 2006 [37]. However, the computing units, such as the number of logic cells and DSP slices, are relatively inadequate.

[1]https://casper.berkeley.edu.

TABLE I
Detailed Hardware Configuration of Pulsar Signal Processing Platform

Name	Model	Characteristic
Sampling	HMCAD1511	8-bit high speed
CPU Board	XC7K160T-2FFG676C	Single/ Dual/ Quad 600 DSP slices
Program download	Raspberry Pi-3 B+	2 10G high-speed ethernet Linux system, Real-time Python interface
Cable interface	SFP-H10GB-CU2M	10 Gbps max data rate

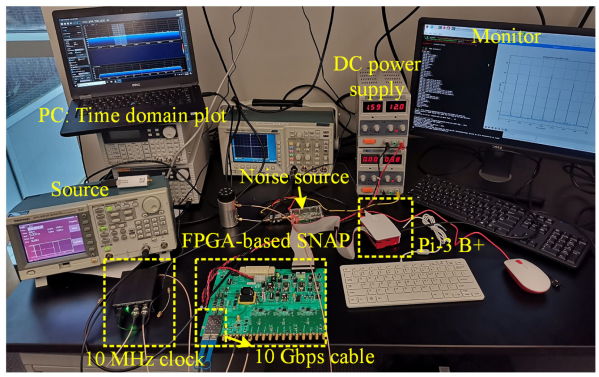

Fig. 2. Pulsar signal acquisition platform based on FPGA.

Here, the latest smart network ADC processor (SNAP)[2] is selected as the motherboard for signal sampling and processing. The SNAP contains three analog devices, and its highest sampling frequency can reach 1000 MHz in a single channel mode. The core of the SNAP is the FPGA XC7K160 T which belongs to Xilinx Kintex7. Compared with the previous hardware platforms, the advantage of selecting is that hardware control is simpler and more integrated. The detailed hardware configuration is listed in Table I. It can be seen that the designed programs can be downloaded via Pi-3, of which the remote real-time debugging is achieved by FTP and Python interface. After the signal is collected, the data can be processed and then transmitted to the server through a 10 Gbps high-speed fiber cable.

The designed FPGA-based DAQ platform is shown in Fig. 2. It shows an empty sample instance when the ADC is not connected to any input. The time domain waveform of the simulated pulse signal can be observed using the PC server. The real-time measurement of the signal spectrum can be observed using the figure in the monitor. To achieve pulsar sampling, the program framework is designed.

C. Hardware Programming and Simulation

In this section, the FPGA programming process is designed to drive the hardware. The software development environment is based on MATLAB 2018a and Xilinx Vivado 2019.1.1 under Ubuntu 16.04. The program can be designed on the Simulink in MATLAB. Utilizing the CASPER toolflow, the Python library

[2]https://casper.ssl.berkeley.edu/wiki/SNAP.

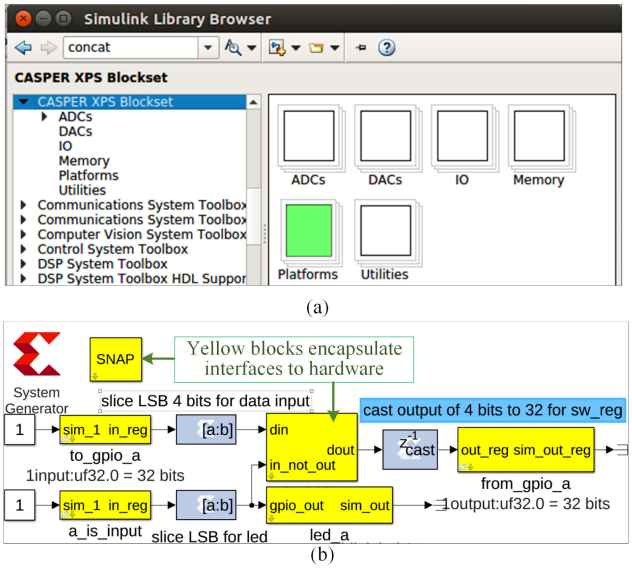

Fig. 3. Software programming environment. (a) The Simulink interface with Xilinx library. (b) The FPGA program example.

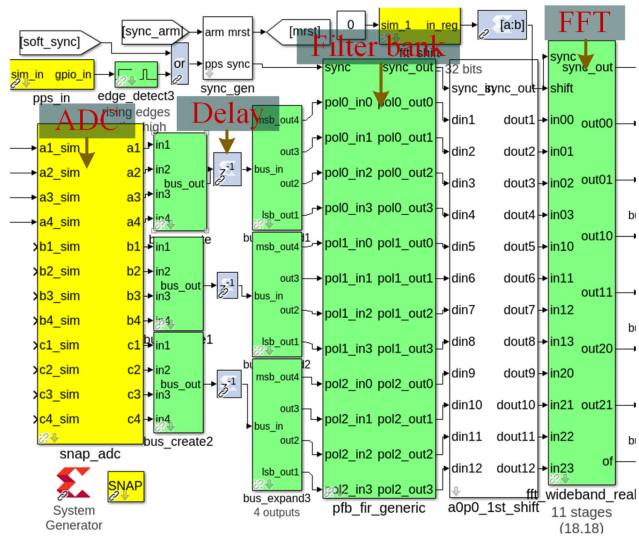

Fig. 4. Program diagram of ADC and PFB module in Simulink.

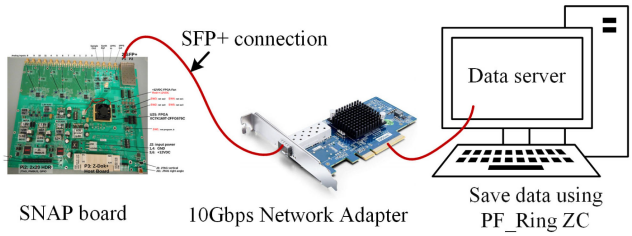

Fig. 5. Hardware structure of data transmission.

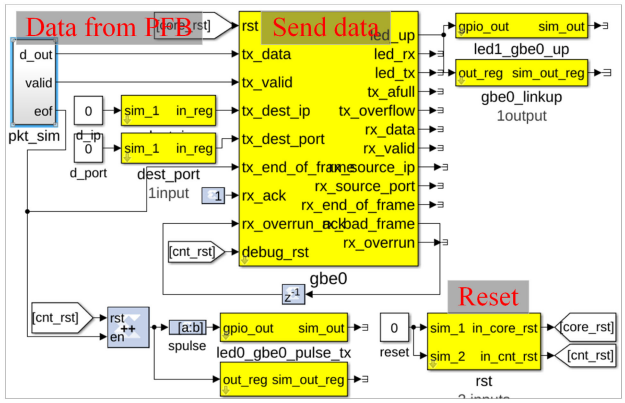

Fig. 6. Program diagram of 10 Gbps module.

casperfpga can be used for further data interaction analysis [38]. The software programming environment is shown in Fig. 3. The software design process can be summarized as

1) Select the required blocks from the Simulink library, as shown in Fig. 3(a).
2) Link different modules as shown in Fig. 3(b) according to the chip datasheet function description.
3) Compile the program and generate an executable file.
4) Configure the FPGA IP address and download the program using Pi-3.

D. Hardware Programming of PFB and 10 Gbps Modules

In the hardware design process, the most important programming modules are polyphase filterbanks (PFB) and 10 Gbps communication. It should be noted that the PFB part can also be performed in the online software program section due to the flexibility of software online design. Here, the detailed structure of the program is described.

The designed program of ADC and PFB parts is shown in Fig. 4. The yellow and green blocks denote the designed program module. The module parameters, such as the sampling rate of ADC and the length of PFB, can be set and converted to verilog language through compilation in Simulink. The data stream is sampled with the 8-bit ADC first, and the sampled data is sent to the filter bank, and finally, the fast fourier transform (FFT) is used to extract the frequency data. The data type of the program, such as the length of data bits, will change with the multiplication and addition operations. The final number of bits output by PFB is 4 to 36 bits. The delay is used to ensure the accuracy of data transmission in Fig. 4.

After the data is processed, the data is transferred to the data server through the 10 Gbps module, whose hardware structure and the designed program are shown in Figs. 5 and 6.

The 10 Gbps module is driven by an on-board 156.25 MHz crystal oscillator. This clock is then multiplied upon the FPGA by a factor of 66, and a single-lane SFP+ connection uses 64b/66b encoding. Thus, the 10 Gbps usable data rate is actually got on the wire. Data for transmitting is first locked into the buffer of the transceiver in 64 b wide words. When the final word of the packet is locked, the transceiver will add a UDP wrapper and begin transmission over IPv4 packets.

To successfully transfer and read data, the transfer process is designed as the following steps, as shown in Fig. 5. After being packed in the SNAP, these packets are then captured at

TABLE II
DATA RATE WITH DIFFERENT DUTIES AND CLOCK FOR 10GBE MODULE

Clock of FPGA	Data rate with different duties/Gbits			
	10%	30%	50%	70%
100 MHz	0.64	1.92	3.2	4.48
200 MHz	1.28	3.84	6.4	8.96

high speed by network adapter X520 on the data server, using PF_Ring ZC (zero copy) technology. It allows the packets to be read directly from the network interface, in which 10 Gpbs wire-rate is achieved at any packet size [29]. Importantly, these configurations are independent of network bandwidth because it does not need to use the network, which means it can work offline. Parsed packet data is finally saved on the hard disk of the data server. This process is driven by the set signal timing and high-speed transmission block which is shown in Fig. 6.

To verify the actual transmission speed of the 10 Gbps module, the relationship between transmission speed and clock frequency of FPGA is tested, where the results are listed in Table II. The duty cycle in Table II determines the word length of each data transmission. For example, the duty cycle cannot exceed 78.125% (156.25/200) when the clock frequency of FPGA is set to 200 MHz, otherwise, the data will overflow. The results also show that the transmission rate can be controlled according to the duty cycle. When the duty cycle is 70%, 8.96 Gbits speed can be reached. According to actual demand, the transmission rate can be adjusted in real-time through the duty cycle.

III. PERIODICAL PULSE EXTRACTION FROM PULSAR SIGNAL

After the hardware design is completed, data processing is critical for the extraction of pulse signals. The collected pulsar signal is very weak and aliased in the noise from the environment. Therefore, the data needs to be processed to obtain stable periodic signals. Denoting the data collected from the telescope as $d(t, c)$, where the t is the sampling time and c is the number of receiver channels, also called polarization. The sampling bandwidth and center frequency of the telescope is set to f_w and f_c, which determine the observation capabilities of radio telescopes. For example, the neutral atomic hydrogen (HI) can only be observed around $f_c = 1420$ MHz [39].

In this section, the PPEM is proposed to obtain the pulsar period from $d(t, c)$, consisting of PFB, incoherent de-dispersion (ID), and sliding window folding. The PFB is responsible for decomposing the pulsar signal into multiple frequency bands. Then, the ID is used to eliminate delays in the results of PFB. Finally, multiple cycles of ID data are superimposed to form a periodic signal in the folding stage.

A. Frequency Extraction Using PFB

The pulse signals are reflected on the frequency axis of $d(t, c)$. In other words, the periodic signal can be obtained on the time axis by dividing the signal on the frequency axis using PFB. Specifically, the PFB can be divided into two parts: A decimating lowpass polyphase filter (DLPF) and discrete fourier transform

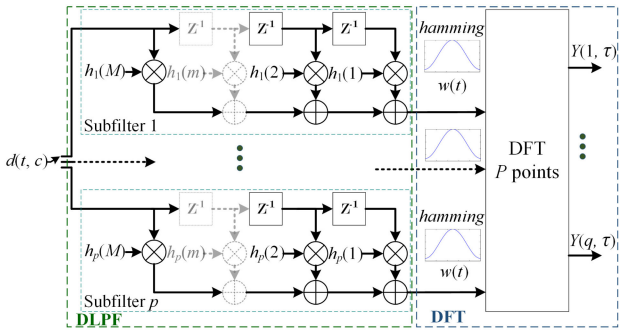

Fig. 7. Primary structure and principle of PFB.

(DFT) [40], [41]. It is noted that some other methods can also be used for pulsar signal processing. For example, the wavelet decomposition can be utilized for the recognition of pulsar signals [42]. However, the PFB is a more efficient and convenient method. The structure and principle of PFB are shown in Fig. 7

In DLPF, the input sequence $d(t, c)$ is decomposed into a set of P subsequences, which can be expressed as

$$y(t,' c) = \sum_{p=0}^{P-1} \sum_{m=0}^{M-1} h_p(m) d(t' - m, c) \tag{1}$$

where the $p \in P, m \in M$, M is the number of polyphase taps (namely the upper summation bound) for each subsequences, $h_p(m)$ is the M coefficients used for weighting in DLPF. Then, the P subsequences are fed into the DFT to get the spectrum Y of each subsequence. The Y can be calculated as

$$Y(k, t,' c) = \sum_{p=0}^{P-1} \sum_{m=0}^{M-1} [h_p(m) e^{-2\pi i k p/P} d(t' - m, c) w(t' - m)] \tag{2}$$

where the $w(t' - m)$ denotes the window function. The hamming window function is used to reduce spectrum leakage.

Then, the $Y(k, t,' c)$ is squared to get the power spectral density. To enhance the signal strength of the time axis, the Y on the polarization channels are further superimposed. The output of PFB becomes

$$Y(q, \tau) = \sum_{i=0}^{c-1} |Y(k, t,' c)|^2 \tag{3}$$

where the q and τ represent q frequency bands and τ time points, respectively. The q can be obtained by $q = n_t/P$, where the n_t is the length of data $d(t, c)$. The relationship between t and τ is $\tau = n_t t/P$. The channel frequency component of different frequency bands become $f_c \pm p(f_w/q)$. The sampling time becomes $t(n_t/n_\tau)$, where the n_τ is the length of data $Y(q, \tau)$. For data with a certain sampling frequency, a higher P means a lower time resolution. Conversely, a lower P means a higher time resolution.

B. ID-Based Delay Calibration

The high radio frequencies emitted by the pulsar travel faster than the lower frequencies. It means that the high radio frequency components arrive earlier, thus affecting the accuracy of in

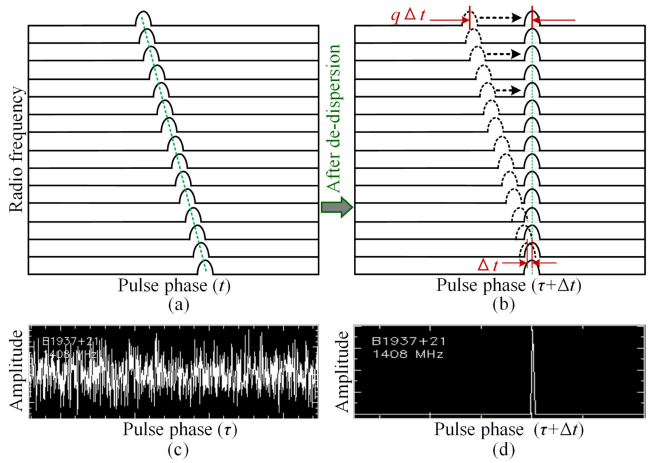

Fig. 8. Incoherent de-dispersion process of pulse. (a) The dispersion in raw pulse. (b) The incoherent de-dispersion of the pulse. (c) The folding of the multiple raw pulses. (d) The folding of the multiple pulses after incoherent de-dispersion.

stage of folding [43]. To eliminate this phenomenon, the ID is presented to compensate for the delay in $Y(q,\tau)$.

The ID calculates the delay Δt difference between different frequency bandwidths. Specifically, this delay Δt can be calculated as [40]

$$\Delta t = e_{dm}(f_{\text{ref}}^{-2} - f_{\text{chan}}^{-2})DM \tag{4}$$

where the $e_{dm} = 4.148808 \times 10^6$ ms denotes the dispersion constant. The f_{ref} and f_{chan} denote the reference frequency and channel frequency in q channel of $Y(q,\tau)$. The units of f_{ref} and f_{chan} are MHz. Here, the f_{ref} can be specified as the center frequency $f_{\text{ref}} = f_c$. The difference in f_{chan} per channel is $\Delta f_{\text{chan}} = f_w/q$. The DM denotes the dispersion measure, which is the density of electrons along the line of sight. It can be obtained as

$$DM = \int_0^d n_e \mathrm{d}l \tag{5}$$

where the d is the distance between the pulsar and Earth. The n_e is the electron number density, it can be approximated as $n_e \sim 0.03\ \text{cm}^{-3}$. The specific DM values can be queried according to the name of pulsars in here[3].

The primary implementation principle of ID is shown in Fig. 8. According to Fig. 8(a), it can be seen that the pulses in different radio frequency channels have a consistent delay. After ID process, Δt delay is added to the pulse phase (time axis). The calibrated data becomes $Y(q,\tau+\Delta t)$, whose different frequency channels are aligned in Fig. 8(b).

C. Sliding Window Folding

In the third stage of the proposed PPEM, the objective of folding is to extract as accurate pulses as possible. Since the background noise of $Y(q,\tau+\Delta t)$ is mostly white noise, the primary idea of folding is to decrease the noise intensity with each other through superposition.

[3]https://www.atnf.csiro.au/research/pulsar/psrcat/

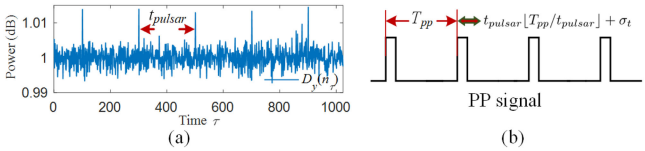

Fig. 9. PP signal generation principle. (a) The result of pulse signal after the PPEM. (b) The PP signal.

To enhance the intensity of the pulse while decreasing the noise, a sliding window folding is introduced to extract the pulse signal. Concretely, sliding window folding can be summarized in the following steps

1) Take the first window. Set the window length of the sliding window as l. The number of pulse period corresponding to l is lT/Pt_{pulsar}, where the t_{pulsar} is the period of the pulsar, T is the total sampling period. The phase of the j^{th} sample becomes $j\tau = jn_t t/P$.
2) Take the next window. Set the window interval to s. Then find the window which has the closest phase to the first sample w_0, where $w_n, n \in Z$ (Integer) is the window sample.
3) Repeat the steps 1) and 2) and find multiple window samples with stride s until the pulse signal strength is much higher than the noise. The result of folding n_τ equals $n_\tau = 1/n \sum_0^n w_n$.

Thereafter, the intensity difference between pulse and noise can be observed using the gain ratio (dB) which can be expressed as

$$D_y(n_\tau) = 10\lg(n_\tau). \tag{6}$$

An example of folding can be seen in Fig. 8(c) and (d). The folding result of the raw pulsar signal does not contain any pulse signals. However, once multiple pulses are aligned and superimposed, the pulse signal becomes apparent as shown in Fig. 8(d).

D. Periodic Pulse Signal Generation

After PPEM, the PP signal can be implemented using the periodic signals n_τ. As shown in Fig. 9, the maximum value is the pulse position. The relationship between the number of pulse and PP signal is

$$T_{pp} = t_{\text{pulsar}}\lfloor T_{pp}/t_{\text{pulsar}} \rfloor + \sigma_t \tag{7}$$

where the $\lfloor\rfloor$ denotes the round down function, and the σ_t is the remaining time deviation. It refers to the PPS signal when T_{pp} equals 1 s.

To obtain an accurate PP signal, linear interpolation based on the pulse period and sampling points is used to estimate σ_t. The PP can be generated at sampling point $n_{\text{pp}} = f_{\text{samp}}T_{pp}$, where the f_{samp} is the sampling frequency. To improve the accuracy of PPS, a more detailed design will be implemented in future work, including the number of foldings, the number of pulse cycles contained in each sliding window.

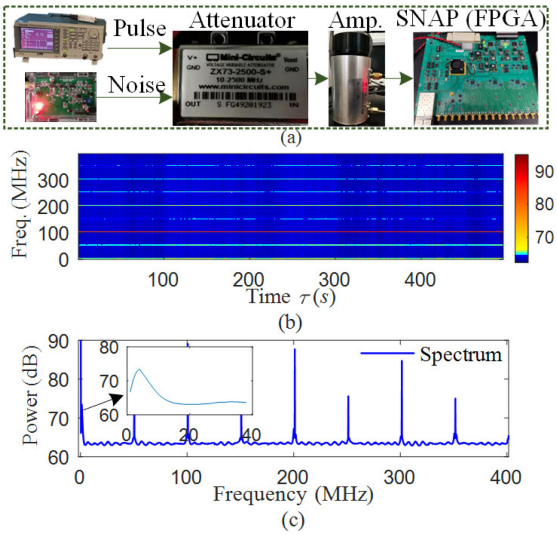

Fig. 10. Spectrum experiments using the FPGA-based DS platform. (a) FPGA-based DS platform. (b) The spectrogram (time versus frequency) result of the simulated pulse signal. (c) The spectrum results from a frequency perspective.

IV. Experiment

To verify the feasibility of the proposed framework, three experiments are performed including the spectrum analysis of the FPGA-based DAQ platform and pulse signal extraction from B0329+54 and B1937+21 pulsars. The B0329+54 pulsar is a second pulsar with a period of 0.715 s. The B1937+21 is a millisecond pulsar with a period of 1.557 ms.

A. Spectrum Analysis

In the first experiment, the spectrum analysis is conducted to verify hardware availability. As demonstrated in Fig. 10(a), the pulse and noise source are first aliased using the digital attenuator. Then the signal strength is adjusted through the manual amplitude adjuster to avoid excessive voltage. After the signal is acquired by the SNAP, the Pi-3 is further used to read and analyze the spectrum of the sampled data. Here, a 1 MHz square wave signal is used as a pulse signal.

Fig. 10(b) shows the spectrogram results of the pulse data over time. It can be seen that there is no obvious pulse information if observed from the time perspective. Meanwhile, the corresponding spectrum signal is shown in Fig. 10(c), which shows multiple obvious frequency components. The frequency component of the pulse signal is slightly weak because the power of the superimposed noise is high. Additionally, some fixed interval frequencies can be observed from Fig. 10(c), which is caused by the mismatch error during the sampling process in ADC. The spectrum results show that the designed FPGA-based DAQ platform can effectively collect and analyze data.

B. Simulation Signal Analysis

To compare with the simulation results, the simulation experiment using the simulated triangle pulse signal is conducted. In this experiment, the arbitrary triangle pulse is generated using the signal source with a frequency of 100 Hz. The sampling frequency of SNAP is set to $f_{\text{samp}} = 60$ MHz. $M = 4$ taps and $q = 1024$ channels are set for the PFB calculated. Since there is no dispersion, therefore the ID calculation is not required. A 24.87-second data are sampled and processed. The detected result is shown in Fig. 10.

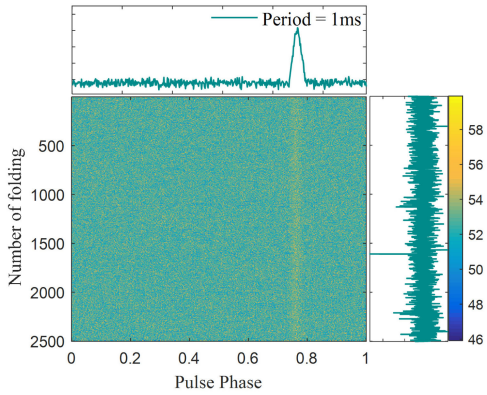

Fig. 11. Extracted pulse using the arbitrary signal.

It can be seen that the triangle pulse has been successfully extracted. The current error is less than 6.8610^{-7} s ($q/f_{\text{samp}}/24.87$ s) by judging whether the maximum point of the pulse has moved. Obviously, less data often corresponds to greater error. Additionally, the pulse is generated using the signal source, which has lower accuracy (± 1 uHz in one year) compared with most of the pulsars. Overall, the accuracy of the simulation results is relatively lower than pulsar where the error comes from the signal source itself and the number of folding times.

C. Second Pulse Signal Extraction

To verify the effectiveness of the proposed PPEM, the pulse extraction experiment is performed. In this section, the period and DM of B0329+54[4] are $t_{\text{pulsar}} = 714.519699726$ ms and 26.7641 cm^{-3} pc, respectively. The f_c and f_w are 7720 and 188 MHz. The f_{samp} is 0.3662 MHz. The window parameters l and s are set to 2045 and 2044, respectively. $q = 512$ channels are used in PFB. Some other parameters are $c = 2$, $T = 1.002$ minutes. The total length of the sample is $n_t = 172032$.

The results of PFB is present in Fig. 12. It shows that the raw signal has been split into multiple frequency channels. From the time axis of Fig. 12, it demonstrates no obvious pulses after the pulsar signal passes through the PFB due to its faintness. Thus the ID is applied to eliminate delays in PFB results.

Thereafter, the pulse signals can be obtained by superimposing PFB results, in which the sliding window folding result is presented in Fig. 13. It can be seen that the pulse signal becomes noticeable after folding. In Fig. 13(a), the pulsar signal is not obvious when the number of folding is 10. When the number of folding is increased to 70, the pulse signal intensity becomes prominent. The power of D_y has reached the 107.05 dB which is much higher than noise. The results show that the sliding

[4]http://seti.berkeley.edu/opendata.

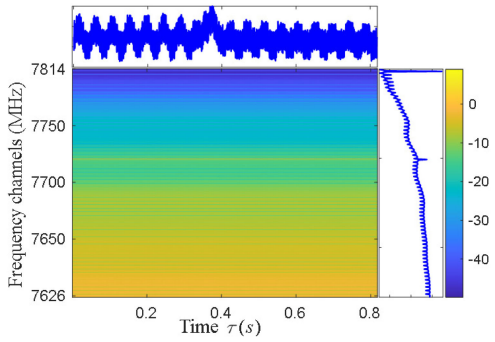

Fig. 12. PFB result of raw pulsar signal for B0329+54. The subplots on the horizontal and vertical axis are the averages from the time and frequency axis, respectively.

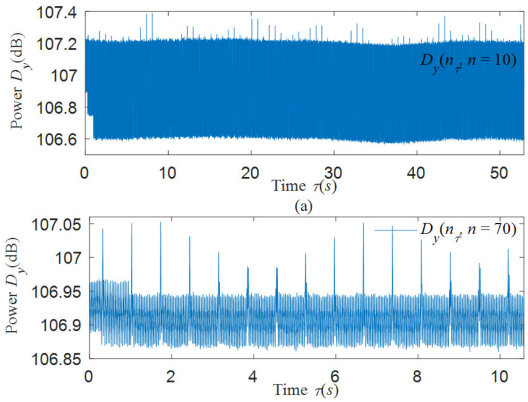

Fig. 13. Results of the proposed PPEM. (a) The result of pulse signal when the number of windows $n = 10$. (b) The result of pulse signal when the number of windows $n = 70$.

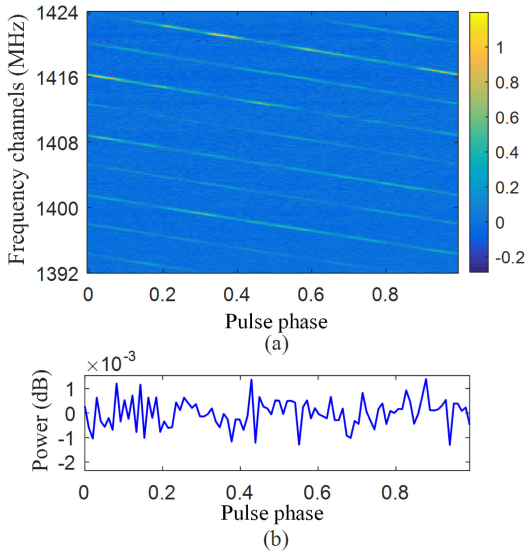

Fig. 14. PPEM results of pulse signal for B1937+21 before de-dispersion.

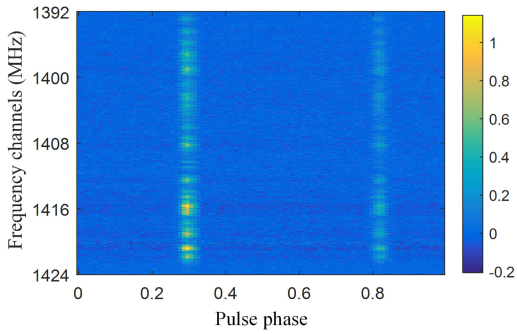

Fig. 15. PPEM results of pulse signal for B1937+21 when the number of windows $n = 382886$.

window folding helps to improve the SNR difference between noise and pulse.

Utilizing the extracted periodic signal, the PP signals can be obtained with an absolute error of 10^{-4} s. The accuracy of PP can be improved by optimizing the parameters of PPEM. To achieve the grid synchronization signal, a time distribution system such as that associated with IEEE 1588.C3 is advocated. This 1588 - precision time protocol (PTP) protocol aligns temporally with the high accuracy, reliability for the PMUs, and related measurement devices. The single link synchronization test error can be reached to 5 ns as reported in [44]. This error is also pretty lower and can meet the minimum requirement for the time error $\pm 26\mu$ s of the PPS in a 60 Hz power system.

Due to the difference in pulsar rotation, the life cycle of different pulsars is also different. A slowly rotating pulsar (close to the end of its life cycle) usually has a large accuracy deviation [45]. Therefore, the millisecond pulsar is preferentially selected as the primary pulsar in the pulsar astronomy-based timing system because its rotation is more stable.

D. Millisecond Pulse Signal Extraction

Besides the second-level pulsar, the signal from a millisecond-level pulsar of B1937+21 is used to extracted PP signal. The B1937+21 is a type of binary pulsars, which has two pulses. The binary pulsar has a binary companion that always belongs to a white dwarf or neutron star. For this pulsar, the period and DM of B1937+21 are $t_{\text{pulsar}} = 1.557806561$ ms and 71.0237 cm^{-3} pc, respectively.[5] The f_c and f_w are 1408 and 32 MHz. The f_{samp} is 64 MHz. The window parameters l and s are set to 98 and 97, respectively. $q = 512$ channels are used in PFB. Some other parameters are $c = 2$, $T = 0.016$ ms. The total duration of the sample is about 596.5 s.

To show the delay scene due to the space medium, the PFB results of the raw pulsar signal for B1937+21 is added and depicted in Fig. 14. As can be seen from Fig. 14(a), it shows that the pulse (yellow color) is not aligned from the time axis. And the higher frequency channel arrives early. This reason is that the transmission speed of different frequency components is different. The average value of the time axis is depicted in Fig. 14(b). Clearly, no pulse can be extracted due to this delay. This phenomenon can be solved by dispersion. Therefore, de-dispersion is necessary for PFB results.

The PPEM result of binary pulsar B1937+21 is shown in Fig. 15. The PFB result has been calibrated using the ID so that

[5]https://www.atnf.csiro.au/research/pulsar/psrcat/.

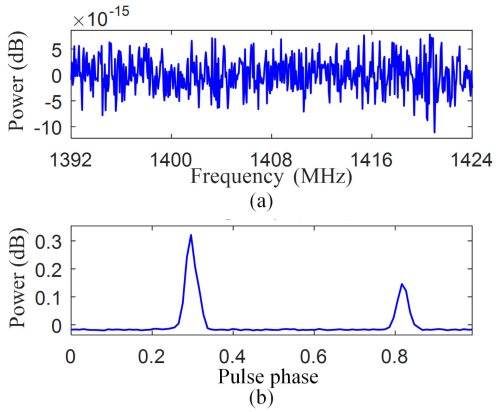

Fig. 16. Average results of the time and frequency channels axis in the results PPEM (Fig. 15). (a) The average result of frequency channels axis. (b) The average result of the time axis, it is the extracted pulses in one cycle.

the lines are aligned in the phase bins (time). It is observed that there are two lines in the PPEM result from the time axis, which means that the binary pulse has been successfully detected. Meanwhile, the strength of some pulse data is weaker than the frequency channels. This is because not every pulse period can be accurately observed by the radio telescope.

To obtain the pulse signal, the average results of the time and frequency channels axis are calculated, as shown in Fig. 16. It can be seen from Fig. 16(a) that there are many noises evenly distributed in different bandwidths in terms of the frequency domain. In Fig. 16(b), it demonstrates that the binary pulse has become obvious after the folding. According to the time resolution of each phase bin, the detected pulse period is about 1.55792 ms, where the absolute error is approximately 26.69×10^{-9} s, which is far lower than the second pulsar. More importantly, when the data length is longer, the accuracy would be better according to [46]. For example, the 10^{-12} s and 10^{-13} s error are obtained for one-day data and one-month data of pulsar J1713+0747, respectively. Therefore, the absolute error of the B1937+21 would be higher if longer time data can be obtained.

V. Conclusion

In this article, a novel pulsar-based timing method is proposed to improve the accuracy of grid synchronization. Moreover, a high-speed signal sampling FPGA-based platform is constructed to process and transmit pulsar data. The experimental test results show the effectiveness of sampling and real-time transmission. The PPEM is proposed to obtain high-precision PP signals. The experiments based on the pulsar signal from B0329+54 and B1937+21 show that the pulsar periodic signals can be accurately extracted using the proposed framework. This framework has the potential to provide accurate and secure clock information for grid synchronization with less than 100 ns timing error when 10 min of data is used. And this error can be lower than the GPS timing signal if longer data are used. Future work will focus on two aspects of further improvement, including the joint debugger between FPGA-based hardware and radio telescopes, and the optimization of the PPEM.

References

[1] Y. Chen, W. Tian, L. Yin, and J. Wang, "Integrated time-frequency synchronisation method for cooperative bistatic radar," *J. Eng.*, vol. 2019, no. 19, pp. 6008–6011, 2019.
[2] D. C. Mazur, R. A. Entzminger, J. A. Kay, and P. A. Morell, "Time synchronization mechanisms for the industrial marketplace," *IEEE Trans. Ind. Appl.*, vol. 53, no. 1, pp. 39–46, Jan./Feb. 2017.
[3] Y. Fan, Z. Zhang, M. Trinkle, A. D. Dimitrovski, J. B. Song, and H. Li, "A cross-layer defense mechanism against GPS spoofing attacks on PMUs in smart grids," *IEEE Trans. Smart Grid*, vol. 6, no. 6, pp. 2659–2668, Nov. 2015.
[4] A. Ranganathan, H. Ólafsdóttir, and S. Capkun, "Spree: A spoofing resistant GPS receiver," in *Proc. 22nd Ann. Int. Conf. Mobile Comput. Netw., ser. MobiCom '16*. New York, NY, USA: Assoc. Comput. Mach., Mar. 2016, pp. 348–360. [Online]. Available: https://doi.org/10.1145/2973750.2973753
[5] M. L. Psiaki, T. E. Humphreys, and B. Stauffer, "Attackers can spoof navigation signals without our knowledge. here's how to fight back GPS lies," *IEEE Spectr.*, vol. 53, no. 8, pp. 26–53, Aug. 2016.
[6] H. Esteban, J. Palacio, F. J. Galindo, T. Feldmann, A. Bauch, and D. Piester, "Improved GPS-based time link calibration involving ROA and PTB," *IEEE Trans. Ultrason., Ferroelectr., Freq. Control*, vol. 57, no. 3, pp. 714–720, Mar. 2010.
[7] S. H. Lee, D. Choi, and J. Park, "Inertia-free stand-alone microgrid-part i: Analysis on synchronized GPS time-based control and operation," *IEEE Trans. Ind. Appl.*, vol. 54, no. 5, pp. 4048–4059, Oct. 2018.
[8] Y. Liu *et al.*, "Wide-area-measurement system development at the distribution level: An fnet/grideye example," *IEEE Trans. Power Del.*, vol. 31, no. 2, pp. 721–731, Apr. 2016.
[9] X. Niu *et al.*, "Quality evaluation of the pulse per second (PPS) signals from commercial GNSS receivers," *GPS Solutions*, pp. 141–150, 2015.
[10] W. Qiu, Q. Tang, K. Zhu, W. Wang, Y. Liu, and W. Yao, "Detection of synchrophasor false data injection attack using feature interactive network," *IEEE Trans. Smart Grid*, vol. 12, no. 1, pp. 659–670, Jan. 2021.
[11] W. Yao *et al.*, "Impact of GPS signal loss and its mitigation in power system synchronized measurement devices," *IEEE Trans. Smart Grid*, vol. 9, no. 2, pp. 1141–1149, Mar. 2018.
[12] S. Thlert, U. Grunert, H. Denks, and J. Furthner, "Absolute calibration of time receivers with DLR's GPS/Galileo HW simulator," in *Proc. 39th Precise Time Time Interval Meeting*, 2007, pp. 323–330.
[13] B. P. B. Elwischger, S. Thoelert, M. Suess, and J. Furthner, "Absolute calibration of dual frequency timing receivers for galileo," in *Proc. Eur. Navigation Conf.*, Apr. 2013, pp. 23–25.
[14] A. Proia, G. Cibiel, and L. Yaigre, "Time stability and electrical delay comparison of dual frequency GPS receivers," in *Proc. 44th Annu. Precise Time Time Interval Meeting*, 2012, pp. 297–302.
[15] R. Priz *et al.*, "Relative calibration of galileo receivers within the time validation facility (TVF)," in *Proc. Joint Conf. IEEE Int. Freq. Control Symp. Eur. Freq. Time Forum*, Apr. 2015, pp. 245–249.
[16] P. Defraigne, W. Aerts, G. Cerretto, E. Cantoni, and J. Sleewaegen, "Calibration of galileo signals for time metrology," *IEEE Trans. Ultrason. Ferroelectr. Freq. Control*, vol. 61, no. 12, pp. 1967–1975, Dec. 2014.
[17] Z. Jiang, D. Piester, and K. Liang, "Restoring a TWSTFT calibration with a GPS bridge-a standard procedure for UTC time transfer," in *Proc. EFTF-2010 24th Eur. Freq. Time Forum*, Apr. 2010, pp. 1–6.
[18] L. Zhan, Y. Liu, W. Yao, J. Zhao, and Y. Liu, "Utilization of chip-scale atomic clock for synchrophasor measurements," *IEEE Trans. Power Del.*, vol. 31, no. 5, pp. 2299–2300, Oct. 2016.
[19] S. Bhamidipati, K. J. Kim, H. Sun, and P. V. Orlik, "GPS spoofing detection and mitigation in PMUS using distributed multiple directional antennas," in *Proc. ICC 2019-2019 IEEE Int. Conf. Commun.*, 2019, pp. 1–7.
[20] Y. Guo, L. Miao, and Xi. Zhang, "Spoofing detection and mitigation in a multi-correlator GPS receiver based on the maximum likelihood principle," *Sensors*, vol. 19, no. 1, p. 37, 2019.
[21] R. N. Manchester, "The parkes pulsar timing array," *Chin. J. Astron. Astrophys.*, vol. 6, no. S2, pp. 139–147, Oct. 2006.
[22] D. Chakrabarty, "Nuclear-powered millisecond pulsars and the maximum spin frequency of neutron stars," *Nature*, vol. 424, pp. 42–44, Jul. 2003.
[23] D. Li *et al.*, "The five-hundred-meter aperture spherical radio telescope (fast) project," in *Proc. Int. Topical Meeting Microw. Photon.*, 2015, pp. 1–3.
[24] M. A. Bowen, R. G. Gough, and M. M. McKinnon, "Receiver systems for square kilometre array survey," in *Proc. 1st Australian Microw. Symp.*, 2014, pp. 47–48.

[25] D. R. DeBoer *et al.*, "The hydrogen epoch of reionization array (hera)," in *Proc. USNC-URSI Radio Sci. Meeting (Joint with AP-S Symposium)*, 2015, pp. 360–360.
[26] J. Hickish *et al.*, "A decade of developing radio-astronomy instrumentation using CASPER open-source technology," *J. Astronomical Instrum.*, vol. 05, no. 04, 2016, Art. no. 1641001.
[27] "American Meteorological Society Policy Program, Satellite Navigation & Space Weather: Understanding the Vulnerability & Building Resilience," *Policy Workshop Report. Amer. Meteorol. Soc.*, Washington, D. C. [Online]. Available: http://www2.ametsoc.org/ams/assets/File/spacWx_GPS_2010.pdf
[28] H. Yin *et al.*, "Pulsar based alternative timing source for grid synchronization and operation," *IEEE Access*, vol. 8, pp. 147818–147826, 2020.
[29] S. Chen, G. Liu, X. Chen, T. Lin, X. Liu, and Z. Duan, "Compact dual-band gps microstrip antenna using multilayer LTCC substrate," *IEEE Antennas Wireless Propag. Lett.*, vol. 9, pp. 421–423, May. 2010.
[30] K. O' Neil,"The green bank observatory - current status," 32nd URSI GASS, Montreal, Aug., 2017, pp. 1–4. [Online]. Available: https://greenbankobservatory.org/science/telescopes/gbt/
[31] "100m Robert C. Byrd Green Bank Telescope," [Online]. Available: https://greenbankobservatory.org/science/telescopes/gbt/
[32] C. Vidal, "Pulsar positioning system: A quest for evidence of extraterrestrial engineering," *Int. J. Astrobiol.*, vol. 18, no. 3, pp. 213–234, 2019.
[33] P.-T. Chen, J. L. Speyer, and W. A. Majid, "Experimental verification of a pulsar-based positioning system using l-band measurements," *J. Guid. Control Dyn.*, vol. 43, no. 1, pp. 60–72, 2020.
[34] *IEEE Standard for Synchrophasor Data Transfer for Power Systems*, IEEE Standard C37.118.2-2011 (Revision of IEEE Std C37.118-2005), pp. 1–53, Dec. 2011.
[35] W. Qiu *et al.*, "Pulsar based timing for grid synchronization," in *Proc. IEEE Ind. Appl. Soc. Annu. Meeting*, Detroit, Michigan, USA, 2020, pp. 1–5.
[36] A. Parsons *et al.*, "A scalable correlator architecture based on modular FPGA hardware, reuseable gateware, and data packetization," *Pub. Astronomical Soc. Pacific*, vol. 120, no. 873, pp. 1207–1221, Nov. 2008.
[37] A. Alvear *et al.*, "FPGA-based digital signal processing for the next generation radio astronomy instruments: Ultra-pure sideband separation and polarization detection," in *Proc. Millimeter Submillimeter Far-Infrared Detectors Instrum. Astron. VIII*, vol. 9914, *Int. Soc. Opt. Photon. SPIE*, 2016, pp. 332–345.
[38] S. Gordon *et al.*, "An open source FPGA-based lekid readout for blast-tng: Pre-flight results," *J. Astronomical Instrum.*, vol. 05, no. 04, 2016, Art. no. 1641003.
[39] Andrew G. Lyne, F. GrahamSmith, and Sir Francis GrahamSmith, *Pulsar Astronomy*, 3rd ed. Cambridge, UK: Cambridge Univ. Press, 2006.
[40] D. R. Lorimer and M. Kramer, *Handbook of Pulsar Astronomy*. Cambridge, UK: Cambridge Univ. Press, 2004, vol. 4.
[41] S. Gowda, A. Parsons, R. Jarnot, and D. Werthimer, "Automated placement for parallelized FPGA FFTS," in *Proc. IEEE 19th Annu. Int. Symp. Field-Programmable Custom Comput. Mach.*, 2011, pp. 206–209.
[42] H. Shan *et al.*, "Wavelet based recognition for pulsar signals," *Astron. Comput.*, vol. 11, pp. 55–63, 2015. [Online]. Available: http://www.sciencedirect.com/science/article/pii/S2213133715000219
[43] B. R. Barsdell, M. Bailes, D. G. Barnes, and C. J. Fluke, "Accelerating incoherent dedispersion," *Monthly Notices Roy. Astronomical Soc.*, vol. 422, no. 1, pp. 379–392, 04 2012. [Online]. Available: https://doi.org/10.1111/j.1365-2966.2012.20622.x
[44] A. E. Tan, *IEEE 1588 Precision Time Protocol Time Synchronization Performance*, *National Semiconductor, Application Note 1728*, Oct. 2007.
[45] F. B. Bernard and F. Graham-Smith, *An Introduction to Radio Astronomy*, 3rd ed. Cambridge, UK: Cambridge Univ. Press, 2009.
[46] P. Chen, "Pulsar-based navigation and timing: Analysis and estimation," University of California (UCLA), Los Angeles, CA, ProQuest Dissertations Publishing, 2018.